PHYSICAL REVIEW B **95**, 045416 (2017)

Spatially indirect exciton condensate phases in double bilayer graphene

Jung-Jung Su[1,*] and Allan H. MacDonald[2,†]
[1]*Department of Electrophysics, National Chiao Tung University, Hsinchu 300, Taiwan*
[2]*Department of Physics and Center for Complex Quantum Systems, University of Texas at Austin, Austin, Texas 78712, USA*

(Received 12 April 2016; revised manuscript received 18 November 2016; published 18 January 2017)

We present a theory of spatially indirect exciton condensate states in systems composed of a pair of electrically isolated Bernal graphene bilayers. The ground-state phase diagram in a two-dimensional displacement-field/inter-bilayer-bias space includes layer-polarized semiconductors, spin-density-wave states, exciton condensates, and states with mixed excitonic and spin order. We find that two different condensate states, distinguished by a chirality index, are stable under different electrical control conditions.

DOI: 10.1103/PhysRevB.95.045416

I. INTRODUCTION

Bernal stacked bilayer graphene is [1] a two-dimensional semiconductor with an electrically tunable band gap that can be as large as ∼250 meV [2–8] when external gates are used to apply a large displacement field perpendicular to the graphene planes. The optical spectrum of bilayer graphene features [9–11] strong and atypical excitonic features. The exciton binding energy increases along with the band gap in strong displacement fields and can be as large as tens of meVs. When two graphene bilayers are placed in close proximity, spatially indirect excitons typically exist as elementary excitations, but can also be present in the ground state under relatively easily established gating conditions. Our main interest in this paper is in constructing a phase diagram for double bilayer graphene systems in the absence of a magnetic field that incorporates the possibility of equilibrium condensation of spatially indirect excitons.

Spatially indirect exciton condensates have a surprising and fundamentally interesting suite of anomalous transport properties that previously have been studied [12,13] only in semiconductor-quantum-well bilayers and only in the quantum Hall regime. They are counterflow superfluids and exhibit, among other properties, spontaneous phase coherence between electrically isolated subsystems. These condensates can be manipulated by external electrical contacts [14–17] via an excitonic generalization of Andreev scattering. Excitonic superflow is manifested most explicitly in a variety of transport experiments [18,19], in which the electrically isolated two-dimensional electron systems are contacted independently.

In the quantum Hall regime, the dissipationless flow of quasiparticle charges in chiral edge channels plays an essential role in determining how excitonic and charged quasiparticle currents interact with external bias voltages. In addition it appears [20] that for currently available quantum Hall bilayer superfluids, disorder also has a large impact on certain quantitative aspects of the observed phenomena. If spatially indirect exciton condensation could be achieved in the absence of a magnetic field, the absence of edge states would introduce fundamentally interesting differences. In particular, it seems likely that disorder could play a less essential role, facilitating more quantitative comparisons between theory and experiment. Double bilayer graphene is an attractive system for efforts to achieve spatially indirect exciton condensation because the energy gaps in each bilayer are relatively small, making it easier to electrically induce equilibrium exciton populations, because the properties of each two-dimensional electrical system can be tuned electrically by using gates to vary their internal displacement fields and because great progress has been achieved experimentally in the flexible construction of multilayer graphene systems with very weak disorder.

The physics of bilayer graphene is rich even when only one bilayer is present. The ground state at the charge neutrality point in the absence of an external displacement field is an interesting spin-density-wave state with opposite spin orientations on opposite layers and a very small staggered moment per atom [21,22]. A first-order phase transition [23] occurs near displacement field $E_d \sim 15$ mV/nm from this spin-density-wave state to a layer-polarized two-dimensional semiconductor state without any broken symmetries. At large displacement fields, the semiconductor state gap can be viewed as originating from an avoided crossing between the conduction band of the low electric potential layer and the valence band of the high electric potential layer. The size of the gap is then limited by the strength of interlayer tunneling in the bilayer. The excitons of this semiconductor are unusual [9,11,24–27] because of the Berry phase properties of graphene's two-dimensional Dirac model states and are in this sense similar to the excitons of a topological insulator [28]. The properties of optically excited populations of bilayer graphene excitons which have thermalized and condensed have been studied in previous [25] theoretical work. Our interest, however, is in excitons which are present in thermal equilibrium, and this can be achieved only for spatially indirect excitons and only when two bilayer graphene systems are present and separated by an insulating barrier [29–33].

Spatially indirect excitons generally have smaller binding energies than spatially direct excitons because of the increased separation between electrons and holes. However, their excitation energies can be tuned electrically by using a gate-controlled displacement field to adjust the relative band lineup of the two bilayers. For a fixed spatial separation between bilayers a displacement field qualitatively alters the band structure of each bilayer, adjusting the band gaps and also the exciton energies. The sensitivity of isolated bilayers

---

[*] jungjsu@nctu.edu.tw
[†] macd@physics.utexas.edu

to displacement fields plays an essential role in the physics we explore below. Previous theoretical work [31,32] has highlighted the potential of double bilayer graphene as a spatially indirect exciton system, but assumed simplified parabolic band dispersions for conduction and valence bands and did not explore the consequences either of this displacement-field sensitivity or of broken-symmetry states in isolated bilayers.

The properties of double bilayer systems can be adjusted electrically by using gates to apply a displacement field or by applying a bias voltage between bilayers, as illustrated in Fig. 1. When tunneling between bilayers can be neglected, bias voltages have the advantage that they alter spatially indirect exciton energies without changing the properties of the isolated bilayers. In this paper we do not account for interbilayer tunneling but concentrate instead on establishing the phase diagram of the negligible tunneling limit. The strength of interbilayer tunneling declines exponentially with the number of layers of intervening dielectric, but is sensitive [34] to disorder and to the relative orientations of both graphene bilayers and the hBN barrier layers. An important difference between graphene monolayers and bilayers is that the latter are semiconductors with a gap [35] between conduction and valence bands, whereas the former are gapless. We are interested here in chemical potential differences between bilayers that are smaller than the gap by an amount close to the exciton binding energy, an interval of bias voltage over which direct the interband tunneling rate vanishes in the temperature $T \to 0$ limit when disorder is absent. We therefore expect that in the regime of interest the tunneling-assisted charge equilibration times between bilayers will be substantially larger than those between monolayers ($\sim 10^{-8}$ s for one-layer-thick hBN barriers) [36–38] and probably dominated by electro-luminescence processes. We also expect that the quasiequilibrium approximation we employ, which will be reliable provided that the charge equilibration times exceed thermalization times, which are often smaller than a picosecond [39–41], can be applicable down to the smallest barrier thicknesses in highly perfect samples. The physics of systems in which the quasiequilibrium approximation is not valid lies beyond the scope of the present work, but is interesting and related to phenomena that have been studied in polariton condensate systems [42].

Exciton condensation occurs when the excitation energy needed to create a spatially indirect exciton in a bilayer graphene system has been electrically adjusted to a negative value, leading to a finite density population of excitons in equilibrium. Our results for the phase diagram of double-bilayer graphene are summarized in Fig. 1, which illustrates how the double-bilayer state depends on the displacement field E_d and on the electrical bias energy U_b. The phase diagram in Fig. 1 was calculated for bilayer separation $t_{\text{hBN}} = 0.3$ nm, corresponding to a single layer of hexagonal boron-nitride (hBN) between the bilayers. The corresponding phase diagram for a bilayer separation of $t_{\text{hBN}} = 0.9$ nm, corresponding to the case of three intervening hBN layers, has been calculated as well. We choose to discuss the $t_{\text{hBN}} = 0.3$ nm case first, because the phase diagram is richest at small layer separations. In addition the phase diagram at larger values of t can be very accurately extrapolated from the $t_{\text{hBN}} = 0.3$ nm results using a procedure we explain later.

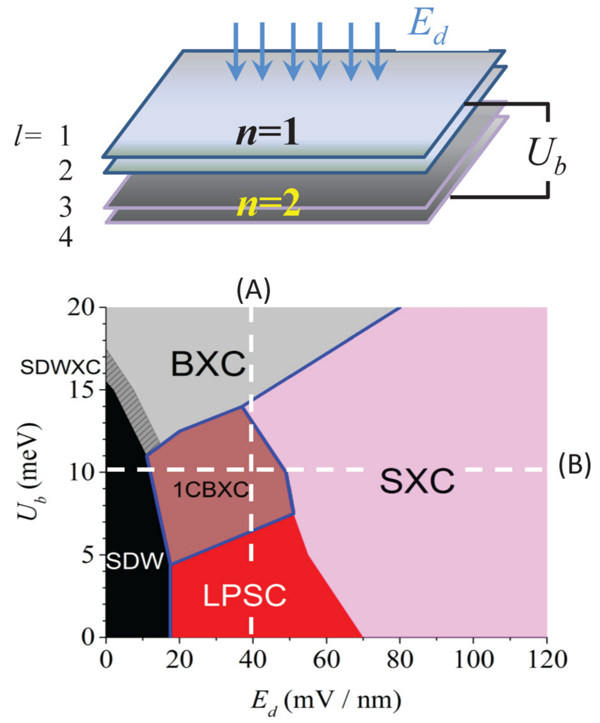

FIG. 1. Upper panel: Schematic illustration of the experimental system modeled in this paper. An external electric field E_d is applied simultaneously to two bilayers (bilayer $n = 1$ with layers $l = 1,2$ and bilayer $n = 2$ with layers $l = 3,4$) by external gates. Separately an electrical bias potential U_b is applied between the two bilayers. In this paper we assume that the leakage current between bilayers is negligible. Lower panel: Mean-field-theory phase diagram of electrically neutral double-bilayer graphene as a function of U_b and E_d. In this paper we have not allowed valley symmetry to be broken. Decoupled bilayers then have a first-order transition between a spin-density-wave (SDW) state at small displacement fields and a layer polarized semiconductor (LPSC) state with no spontaneously broken symmetries at large displacement fields. In double bilayers the LPSC is unstable at large displacement fields E_d to an exciton condensate (SXC) with coherence mainly between the adjacent single layers $l = 2$ and $l = 3$. Excitons can also be induced electrically by applying a bias voltage U_b between bilayers. For large U_b the SDW state is unstable to an exciton condensate (BXC) with coherence mainly between the conduction band of bilayer $n = 2$ and the valence band of bilayer $n = 1$. Within each bilayer the pattern of interlayer coherence is determined by single-particle physics. The differences between the order parameters of the SXC and BXC states, and those of other states with both excitonic and spin order that occur at intermediate values of U_b and E_d, are discussed at length in the main text. The phase boundaries marked by solid blue lines are first order, and the remaining phase transitions are continuous. We explain the physics of the various phase transitions below by closely examining competing states along lines (A) and (B). This phase diagram was constructed for the case of interbilayer separation $t_{\text{hBN}} = 0.6$ nm; t_{hBN} dependence is discussed at length, and the corresponding phase diagram at $t_{\text{hBN}} = 1.2$ nm is presented in the penultimate section of this paper.

We describe the many-exciton state using mean-field theory. We find that for small U_b the two bilayers are uncorrelated, and that they have a first-order transition between a spin-density-wave (SDW) state at small displacement fields E_d and a layer

TABLE I. Acronyms used for distinct electronic states in the main text. The SDW and SDWXC states break time-reversal symmetry. The SXC, BXC, SDWXC, and 1CBXC states break the separate particle-number conservation symmetry of the individual bilayers.

SDW	Spin density wave
LPSC	Layer-polarized semiconductor
SXC	Single-layer exciton condensate
BXC	Bilayer exciton condensate
SDWXC	Spin-density-wave exciton condensate
1CBXC	1-component Bilayer exciton condensate

polarized semiconductor (LPSC) state at larger displacement fields. The LPSC is unstable at still larger E_d to the SXC state in which coherence is established mainly between the adjacent single graphene layers labeled $l = 2$ and $l = 3$. For large U_b and small E_d the SDW state is unstable to the bilayer exciton condensate (BXC) state in which coherence is established mainly between the conduction band of bilayer $n = 2$ and the valence band of bilayer $n = 1$. Among other interesting features that appear in this phase diagram, we find that exciton condensation is sometimes combined with spin-density-wave order, which breaks time-reversal symmetry, and sometimes not, and that excitons condense into different states at large E_d than at large U_b. The phase diagrams at larger t_{hBN}s are discussed in the later sections. The greatest change is that single-layer exciton condensate (SXC) states occur at smaller values of E_d because the external potential difference between the bilayers at a given E_d increases. The reduction in exciton binding energies at larger t_{hBN}s also plays a role. We have summarized the acronyms of states that appear in this paper in Table I.

Note that the mean-field theory does not account for quantum fluctuations in the many-body ground state which are evidenced, for example, by finite drag resistivities in the absence of interlayer coherence. When quantum fluctuations are included, states with interlayer phase coherence can lose their order and form Fermi liquid states, or excitons can pair to form biexcitons. All of these possibilities are discussed at greater length later.

Our paper is organized as follows. In Sec. II we provide some technical details on the mean-field calculation we perform for the four-layer graphene system of interest, the double bilayer. Section III summarize the mean-field theory description of the SDW to LPSC state phase transition in an isolated bilayer, showing that reasonable agreement with experiment follows from a physically sensible approximate treatment of screening that we employ for all subsequent calculations. In Sec. IV we describe in detail how the quasiparticle energy bands and wave functions evolve as E_d is increased at $U_b = 0$. Along this line in the phase diagram, reduction in spatially indirect exciton energy with increasing E_d is accompanied by increasing layer polarization within the individual bilayers. For bilayers separated by a single layer of hBN, we find that the SDW to LPSC phase transition occurs before the indirect exciton energy vanishes and interlayer phase coherence appears. By the time the phase-coherent condensate state appears, the individual bilayers are already strongly polarized and the condensate is dominated by coherence between the most closely spaced layers. In Sec. V we describe in detail how the quasiparticle energy bands and wave functions evolve as U_b is varied at $E_d = 0$. In this case the individual layers have a small gap associated with spin-density-wave order. Condensation then occurs first as an instability of a state with broken time-reversal symmetry. Coherence is strongest between layers 1 and 3 for one spin orientation and between layers 2 and 4 for the other. Upon increasing U_b further, the condensate evolves into the BXC state which is spin-rotationally invariant and allows for charge transfer between the bilayers. In Sec. VI, we discuss lines A and B in the phase diagram of Fig. 1. When E_d and U_b are present, a series of intermediate states can occur along lines which cross between weakly correlated bilayer and either SXC (large E_d) or BXC (large U_b) states. We also present a phase diagram calculated by applying the same considerations to a model with a larger bilayer separation, $t_{\mathrm{hBN}} = 0.9$ nm, and explain how it is related to the $t_{\mathrm{hBN}} = 0.3$ nm phase diagram. Finally, in Sec. VII we comment on the limitations of mean-field theory and speculate on the experimental implications of this study.

II. MEAN-FIELD THEORY OF EXCITON CONDENSATE AND SPIN-DENSITY-WAVE STATES IN DOUBLE BILAYER GRAPHENE

The mean-field theory calculations preformed here neglect the possibility of broken valley symmetry but allow the Hamiltonian's spin-rotational invariance to be broken. We therefore study a 16-band model with π orbitals of both spins on both sublattices of four honeycomb lattice layers. The full mean-field Hamiltonian is $H = H_B + H_{\mathrm{int}}$ where H_B is the single-particle band Hamiltonian and H_{int} describes the Coulomb interaction contribution. The band Hamiltonian can be written down most concisely as

$$H_B(\mathbf{k}) = \{H_{BL}(\mathbf{k}) \otimes \sigma_0 + [U_b + eE_d\,(t_{\mathrm{hBN}} + 2d)]/2 \otimes \sigma_z\} \otimes s_0, \quad (1)$$

where H_{BL} is the band Hamiltonian of an isolated AB-stacked bilayer, $\boldsymbol{\sigma}$ is a Pauli matrix vector that acts on the pseudospin expanded by bilayer 1 and 2 and $\boldsymbol{s}$ is Pauli matrix that acts on the real spin degree of freedom. Here we define d as the separation between layers within a graphene bilayer and t_{hBN} as the increase in the separation between graphene bilayers when they are separated by hBN layers; i.e., it is approximately equal to d times the number of hBN layers that are present.

In the $(1A,1B,2A,2B)$ sublattice representation, the isolated bilayer Hamiltonian is [1]

$$H_{BL}(\mathbf{k}) = \begin{pmatrix} eE_d\,d/2 & \hbar vk\,e^{-i\psi_{\mathbf{k}}} & 0 & 0 \\ \hbar vk\,e^{i\psi_{\mathbf{k}}} & eE_d\,d/2 & \gamma_1 & 0 \\ 0 & \gamma_1 & -eE_d\,d/2 & \hbar vk\,e^{-i\psi_{\mathbf{k}}} \\ 0 & 0 & \hbar vk\,e^{i\psi_{\mathbf{k}}} & -eE_d\,d/2 \end{pmatrix}. \quad (2)$$

Here v is the bare Dirac velocity of an isolated graphene layer, γ_1 is the interlayer hopping parameter, and $\psi_{\mathbf{k}} \equiv \tan^{-1}(k_y/k_x)$.

We will see that the momentum-orientation dependence of the intersublattice hopping term within each graphene layer, which is famously responsible for Berry phase features in the electronic structure of all single and multilayer graphene systems, also plays an important role in determining the double-bilayer phase diagram.

In mean-field theory, Coulomb interactions give rise to self-consistently determined Hartree and exchange self-energies. We separate these contributions, writing $H_{\rm int} = H_H + H_X$, where H_H is the Hartree contribution and H_X accounts for exchange. We use a representation of site-dependent π-band orbitals and label our 16 bands by the compound index $b \equiv \{l,x\}$ where $l = 1\ldots4$ is the layer index and $x = A,B$ is the sublattice index within a layer. With this notation the Hartree term in the mean-field Hamiltonian is

$$\langle b' \,|\, H_H(\mathbf{k})\,|b\rangle = -g\,\delta_{b',b}\frac{2\pi e^2}{\epsilon}\sum_{b''} d_{b,b''}\,n_{b''}. \tag{3}$$

Here the factor $g = 2$ accounts for the two-fold valley degeneracy, the dielectric constant ϵ is that of the embedding material, $d_{bb'}$ is the distance between the layers associated with labels b and b', and n_b is the total carrier density projected onto band b.

The exchange contribution to the mean-field Hamiltonian is responsible for exciton condensation and therefore plays the most essential role in the physics described below.

$$\langle b|\,H_X(\mathbf{k})\,|b'\rangle = -\int \frac{d^2\mathbf{k}'}{(2\pi)^2}\,V_{bb'}(|\mathbf{k}-\mathbf{k}'|)\,\langle b|\,\tilde{\rho}(\mathbf{k}')\,|b'\rangle, \tag{4}$$

where $V_{bb'}(|\mathbf{q}|) = 2\pi e^2\,e^{-q\,d_{bb'}}/\epsilon q$ is the two-dimensional Coulomb interaction between bands b and b'. In evaluating Eq. (4) we employ the regularized density matrix $\tilde{\rho} \equiv \rho - \rho_0$, where ρ_0 is the density matrix for isolated layers with full valence bands and empty conduction bands. In doing so, we take the view that the Dirac velocity parameter of an isolated layer already accounts for exchange interactions with the bare valence band states. Note that coherence between bands gives rise to an interaction-induced interband hopping term in the mean-field Hamiltonian.

The densities and density matrices in Eqs. (3) and (4) must be determined self-consistently. The off-diagonal terms in the density matrices capture the coherence between sites presents in the wave functions of occupied quasiparticle states. Because of the dependence of hopping within each graphene layer on $\psi_{\mathbf{k}} \equiv \tan^{-1}(k_y/k_x)$, the exchange contribution to the Hamiltonian is dependent on both momentum magnitude and orientation. Fortunately, the momentum orientation of the relative phases [43] of quasiparticle projections onto different bands has a very simple form in multilayer graphene:

$$\langle b|\,\tilde{\rho}(\mathbf{k})\,|b'\rangle = f_{bb'}(k)\exp[-i(J_b - J_{b'})\psi_{\mathbf{k}}], \tag{5}$$

where $f_{bb'}(k)$ captures the density-matrix dependence on k and J_b is a band-dependent chirality index which will be discussed at greater length below. With this notation, the exchange contributions to the mean-field Hamiltonian become

$$\langle b|H_X(\mathbf{k})|b'\rangle = -e^{-i(J_b-J_{b'})\psi_{\mathbf{k}}}\int dk'u_{bb'}(k,k')f_{bb'}(k').$$

The interaction factor $u_{b,b'}(k,k')$ is determined by an angular integral which can be evaluated once and for all and used throughout the self-consistent iteration process:

$$u_{b,b'}(k,k') \equiv \frac{k'}{(2\pi)^2}\int d\theta\;V_{bb'}[q(k,k',\theta)]\,e^{-i(J_b-J_{b'})\theta},$$

where $q(k,k',\theta) = [k^2 + k'^2 + 2kk'\cos(\theta)]^{1/2}$. Note that exchange interactions are stronger between bands with nearby layers and more similar chirality indices.

When interactions are neglected, the band-dependent chirality indices J_b in an electrically coupled multilayer graphene system are determined by the stacking sequence [44]. The index can be defined as $J_b \equiv \mathrm{Arg}[\langle\phi\,(\mathbf{k})|b,\mathbf{k}\rangle]/\psi_{\mathbf{k}}$, where $|\phi\,(\mathbf{k})\rangle$ is a site representation Bloch state. Only the relative chirality indices between bands are gauge invariant. For a Bernal bilayer the chirality indices can be read off Eq. (2) by observing that the band eigenstates have momentum orientation dependence of the form $|\phi\rangle = (c_{1A},c_{1B}e^{i\psi_{\mathbf{k}}},c_{2A}e^{i\psi_{\mathbf{k}}},c_{2B}e^{i2\psi_{\mathbf{k}}})$, corresponding to chirality indices $J_{BL} = (0,1,1,2)$ for the four sites $(1A,1B,2A,2B)$.

In a spatially indirect exciton condensate state coherence is spontaneously established between the Coulomb-coupled but electrically isolated bilayers of a double bilayer system. Because the band energy cost of altering band-chirality differences within either bilayer is prohibitive, the band chirality indices in double bilayers are of the form $J_b = J_{BL} + \delta_{n,2}J_X$. (Note that we are free to choose a gauge with $J_X = 0$ for bilayer $n = 1$.) J_X can be viewed as the angular momentum of the spatially indirect excitons that form and is an integer-valued chirality index that distinguishes different excitonic states. Below we describe the properties of quasiparticle states in one graphene valley only, say, valley K. Because we assume that the two valleys are related by time-reversal symmetry, the chirality index of valley K′ is understood to be opposite to that of valley K.

With these conventions the $J_X = -2$ state is one in which the chirality difference between sites $1A$ and $4B$ is zero. The self-consistent state with this choice for J_X therefore has strong coherence between these two sites. Similarly, the $J_X = 0$ state has strong coherence between equivalent sites in the two bilayers. We therefore refer to $J_X = 0$ exciton condensates as bilayer exciton condensates (BXCs). For $J_X = 2$, the chirality indices are identical for the $2B$ and $3A$ sites. We refer to the $J_X = 2$ states as single-layer exciton condensates (SXC). For each many-body state, we calculate total energy density by using

$$E_{\rm tot}/A = \langle H_B\rangle/A + (\langle H_H\rangle + \langle H_X\rangle)/2A, \tag{6}$$

where A is the area of the system. The factor of 2 in Eq. (6) corrects for the double-counting of interactions in the mean-field state. As we explain below the $J_X = 0$ BXC and $J_X = 2$ SXC states compete for the ground state, with the preferred state determined mainly by the influence of the displacement field E_d on layer polarization within the isolated bilayers. The $J_X = -2$ states are never ground states.

It is important to recognize that there are small [45] but nonzero corrections to the minimal π-band model Hamiltonian we have adopted in Eq. (2), for example, the corrections responsible for trigonal warping of constant energy surfaces.

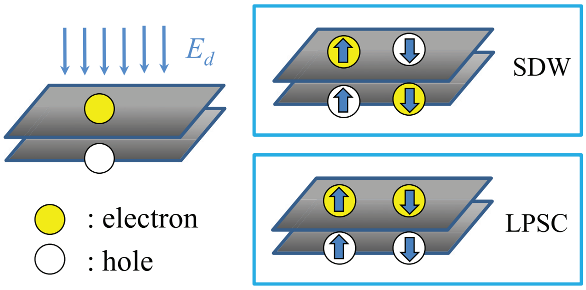

FIG. 2. Schematic illustration of the isolated bilayers states. The competition between spin-density-wave (SDW) and layer polarized semiconductor (LPSC) states can be tuned experimentally by varying the displacement field E_d. The SDW state has broken time-reversal symmetry, whereas the layer-polarized-semiconductor (LPSC) state has no broken symmetries. Both states have energy gaps. The yellow and white circles represent electrons and holes respectively. The arrows in the circles represent spin orientations. In the SDW state, opposite spins have opposite layer polarization, whereas in the LPSC state, the layer polarization is not spin dependent.

When these terms are included, the quasiparticle bands do not have definite chirality indices even at the single-particle level. Because these terms are small, however, we do not expect that they will materially influence the double bilayer phase diagram.

III. INFLUENCE OF A DISPLACEMENT FIELD E_d ON BILAYER GRAPHENE

In this section we discuss the application of mean-field theory to isolated bilayers subject to an applied displacement field E_d. This digression is necessary partly because excitonic states emerge in many cases as instabilities of single-bilayer states that are on their own nontrivial, and partly as a reality check in which our approach is applied to a case in which extensive experimental data are already available. All calculations in this paper were performed using $e^2/2\pi\epsilon = 50$ meV nm, corresponding to $\epsilon \sim 4$, and reducing interaction strengths by a further factor of $C_s = 0.8$ to account for additional screening effects. This value for C_s was chosen phenomenologically to adjust the displacement field at which the SDW to LPSC transition (see below) occurs to $E_d \sim 20$ mV/nm, the value found experimentally by Velasco *et al.* [35].

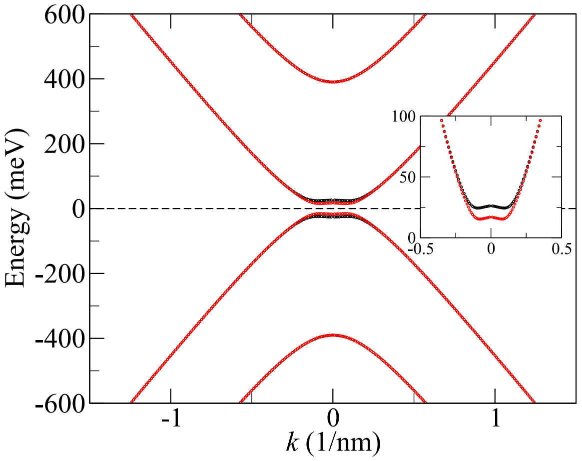

FIG. 3. Typical quasiparticle band dispersions for bilayer graphene at $E_d = 0$. The black and red squares illustrate the quasiparticle energy dispersion of the SDW and LPSC states respectively. The bands of the two states are similar and both have gaps. (See inset.) Interactions dominate at small k because of bilayer graphene's quadratic crossing between valence and conduction bands. The quasiparticle dispersion at large k is not strongly influenced by electron-electron interactions.

It is well established [35,46–55] that at zero magnetic field the stable many-body states in an isolated bilayer graphene system are the spin-density-wave (SDW) and the layer-polarized-semiconductor (LPSC) states illustrated in Fig. 2. In an SDW state, opposite layers have opposite spin polarizations, although each layer is neutral only when $E_d = 0$. The SDW state breaks time-reversal symmetry. The microscopic character of this state is quite distinct from that of a Heisenberg model system on a honeycomb lattice, as signaled by the fact that the staggered moment per atom is very small compared to one Bohr magneton per atom. The scale of the spin polarization is in fact set by the strength of the interlayer tunneling amplitude, which increases the masses of the states at valence and conduction band edges. Because the SDW state has an unfavorable layer polarization for one spin orientation, it becomes unstable at large E_d. The LPSC state, which is the ground state at large E_d, has no broken symmetry when $E_d \neq 0$. Both states exhibit gaps (even for zero E_d) when electron-electron interactions are included, as seen in Fig. 3.

The SDW state has no overall layer polarization at $E_d = 0$, as illustrated in Fig. 4, and is the ground state [56] because it avoids the electrostatic energy associated with spontaneous layer polarization. In our calculations, which do not allow for spontaneous valley polarization, there is an first-order phase transition between SDW and LPSC states at $E_d \sim 17$ mV/nm. In Fig. 4, we plot the mean-field-theory quasiparticle energy gaps versus E_d. The mean-field-theory gap is ∼50 meV at $E_d = 0$ and increases up to 75 meV for $E_d \sim 100$ mV/nm.

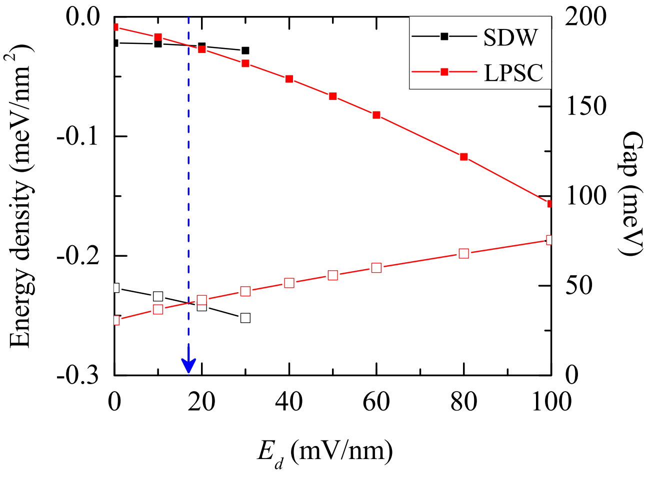

FIG. 4. Total energy and quasiparticle gap vs applied electric field E_d. The black and red closed (open) squares represent the total energy (quasiparticle gap) for SDW and LPSC states respectively. The SDW state is the ground state for small E_d whereas the LPSC becomes the ground state for $E_d \gtrsim 17.0$ mV/nm, as indicated by the blue arrow.

The size of these gaps is strongly enhanced by the nonlocality of exchange interactions, as reflected also by the difference between LDA and GW approximation gaps in *ab initio* theories [24]. The difference is especially strong at small displacement fields, since the gap vanishes at $E_d = 0$ when exchange interactions are neglected. On the other hand, gaps are overestimated when exchange interactions are not screened.

IV. SPATIALLY INDIRECT EXCITON CONDENSATES IN DOUBLE BILAYER GRAPHENE: $U_b = 0$

We begin our exploration of the double bilayer phase diagram by focusing first on the $U_b = 0$ line, first for the case of bilayer separation $t_{\mathrm{hBN}} = 0.3$ nm corresponding to one layer of hexagonal boron-nitride between graphene bilayers. For the double bilayer case we discuss here and later, we use the same set of screening parameters ($\epsilon = 4$ and $C_s = 0.8$) as that in the single bilayer calculation. Although the presence of one bilayer might further screen the other, this additional effect is limited as long as the electron density in each layer is still small, i.e., in the BEC regime. We therefore do not expect the phase boundary calculated to be very strongly altered by additional screening effects [57].

In our calculation, we find that for $E_d \lesssim 70$ mV/nm, the mean-field bilayer state is not altered by the proximity of a neighboring bilayer. Beyond this value of E_d, coherence develops between bilayers, and charge is transferred from the high-potential-energy bilayer to the low-potential-energy bilayer. The critical value of E_d at which spatially indirect coherence first develops can be identified with the displacement field at which the potential drop between bilayers is large enough to tune the lowest energy interbilayer spatially indirect exciton energy to zero.

Whenever isolated excitons have negative energies, their populations build up to finite values fixed by the repulsive [58] exciton-exciton interaction strength, and they condense to yield spontaneous interlayer phase coherence. As explained in Sec. II, the exciton condensate states of double bilayer graphene, and the corresponding isolated exciton states, are distinguished by an interlayer chirality index, J_X. The spontaneous coherence of the $J_X = 2$ state is characterized by a relative phase between the 2B and 3A sites that is momentum orientation independent. This state maximizes the strong electron-hole interactions between π orbitals that are located on these adjacent layers, and we therefore refer to it as the single-layer exciton condensate (SXC) state. Because it produces electrons and holes unevenly within a bilayer, it is naturally layer polarized and takes good advantage of the displacement field within each bilayer to lower its energy. The $J_X = 0$ state, on the other hand, has momentum-orientation-independent interlayer phases between bilayer valence band states shared between layers 1 and 2 and bilayer states shared between layers 3 and 4. For this reason we refer to it as the bilayer exciton condensate (BXC) state. The phase differences are momentum orientation independent between layers 1 and 3 and between layers 2 and 4. Because these layer pairs are further apart than layers 2 and 3, they have weaker electron-hole interactions. Moreover, the $J_X = 0$ BXC state gains most interbilayer exchange energy when it is not layer polarized and is therefore less able to lower its energy in a displacement field. On the other hand it gains more energy from hopping within the individual bilayers. Figure 5 contains a cartoon representation of the coherence patterns within the $J_X = 0$ and $J_X = 2$ states, and Figs. 6 and 7 illustrate their quasiparticle bands and coherence properties.

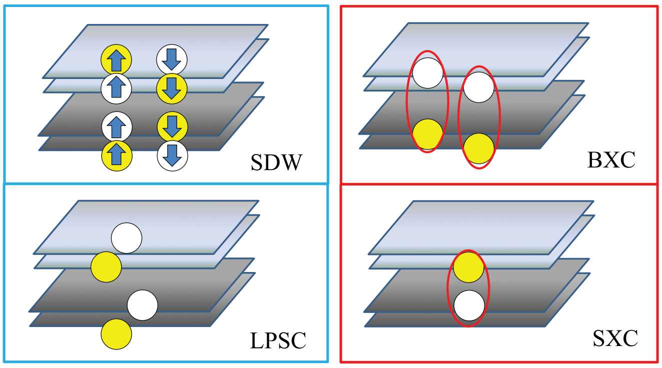

FIG. 5. Cartoon illustration of four double bilayer states: SDW, LPSC, SXC, and BXC. The red circles represent the dominant spontaneous coherence channel, as explained in the main text.

The transition from the LPSC state to an excitonic condensate occurs at $E_d \sim 70$ mV/nm for the bilayer separation studied and is from a state with no broken symmetries to a SXC state, rather than to a BXC state. We now explain the microscopic physics responsible for this choice. The main panel in Fig. 6 compares the quasiparticle dispersions of the SXC and BXC states at $E_d = 80$ mV/nm, inside but close to the boundary of the exciton condensate portion of the phase diagram. (The eight bands plotted are all doubly degenerate because neither the BXC state nor the SXC state break spin-rotational invariance.) We concentrate on the four doubly degenerate quasiparticle bands that are close to the

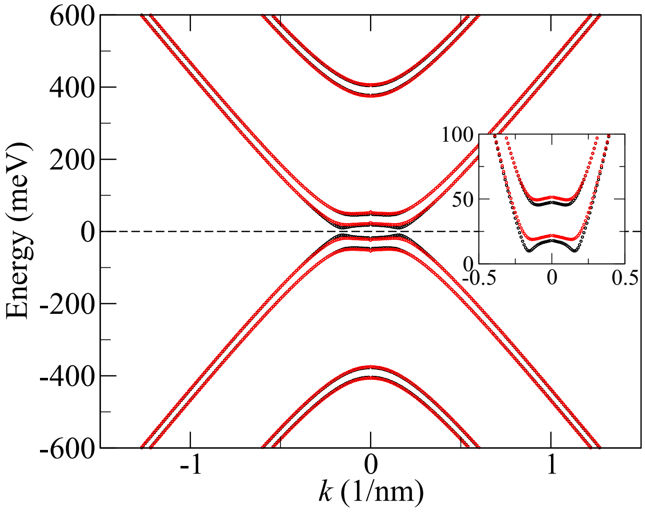

FIG. 6. Quasiparticle dispersions of the single-layer exciton condensate state (SXC, $J_X = 2$) and the bilayer exciton condensate state (BXC, $J_X = 0$) near the boundary between the LPSC and the BXC state at $E_d = 80$ mV/nm and $U_b = 0$. The BXC state is higher in energy because it is less able to polarize charge within each bilayer to take advantage of the displacement field.

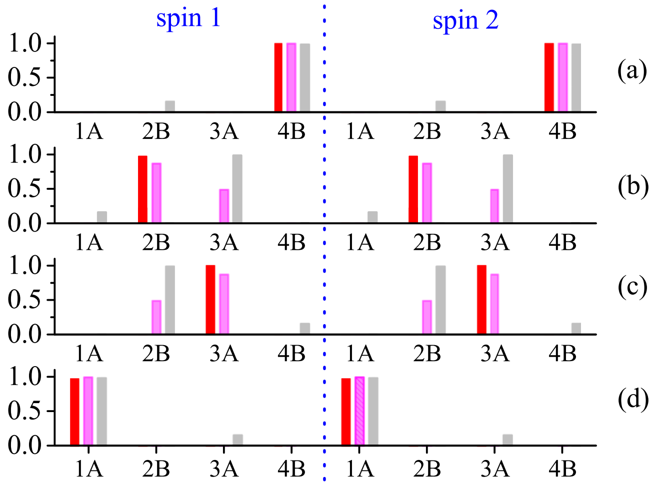

FIG. 7. Band projections of low-energy $k = 0$ eigenstates calculated for $E_d = 80$ mV/nm and $U_b = 0$. Panels (a), (b), (c), and (d) are for the two highest-energy valence band states and the two lowest-energy conduction band states, ordered by increasing eigenenergy. The red, magenta, and gray solid bars represent site projections calculated for the LPSC, SXC, and BXC states respectively. Because none of these states break spin symmetry, the quasiparticles energies are doubly degenerate and the orbital wave functions are spin independent.

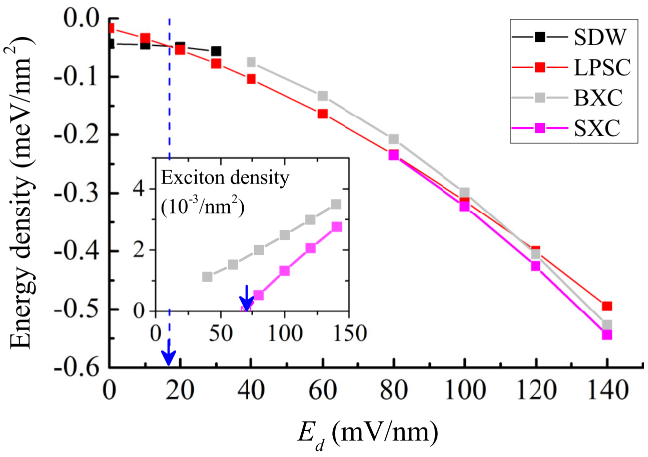

FIG. 8. Total energy vs E_d for SDW, LPSC, SXC, and BXC states. The inset plots the exciton densities of the SXC and BXC states. The SDW is the lowest energy state for small E_d. With increasing E_d the ground state of the system first transforms into the LPSC state via a first-order phase transition and then into the SXC state via a continuous phase transition. These results were obtained for hexagonal boron nitride barrier thickness $t_{\mathrm{hBN}} = 0.3$ nm.

Fermi energy (two above and two below). For large momenta the bands are virtually identical in SXC and BXC states, and approach those of two isolated bilayers with an energy offset equal to the electric potential difference $e(t_{\mathrm{hBN}} + 2d)$ between the two bilayer systems. Differences between SXC and BXC states are found only in the small-k region highlighted in the inset, where we see that the band dispersions are flatter and that the gap is slightly larger in the SXC state.

More information on the low-energy eigenstates can be obtained by projecting them onto the site-localized basis set used for the Hartree-Fock calculations. Figure 7 plots $k = 0$ eigenstates of the eight bands close to the Fermi level project onto A and B sublattice sites at $E_d = 80$ mV/nm and $U_b = 0$. The projections onto 1B, 2A, 3B, and 4A are neglected because these sites have strong single-particle coupling to an adjacent layer and have high weight not in the bands close to the Fermi level, but in the higher energy bands that are further from the Fermi level. Figures 7(a), 7(b), 7(c), and 7(d) are in the order of ascending energy; the projections plotted in Figs. 7(a) and 7(b) are for occupied dressed valence bands while those in Figs. 7(c) and 7(d) are for unoccupied conduction bands. Because spin-rotational symmetry is not broken, the degenerate ↑ and ↓ bands in each panel have identical wave functions. The color codes identify the distinct many-body states: The red, magenta, and gray solid bars are $k = 0$ projections for the LPSC, SXC, and BXC states respectively.

As seen in Fig. 7, the $k = 0$ eigenstates of the LPSC are completely localized in energetic order on sites 4B, 2B, 3A, and 1A. (The degree of layer polarization of the band eigenstates decreases as wave-vector magnitude k increases.) Site 2B is occupied before site 3A, even though layer 3 has a lower external potential than layer 2 because of the exchange-enhanced gap in an isolated bilayer discussed in Sec. III. The SXC state $k = 0$ bands are similar to the LPSC bands in composition, except that the bands closest to the Fermi energy, originally localized on 2B and 3A sites, hybridize. In the BXC state the strongest hybridization occurs between sites whose layer indices differ by 2. Note that layer 3 has higher weight at $k = 0$ than layer 2 in the occupied valence states in the BXC and that the condensation energy associated with excitons is reduced. For this reason the SXC state is always the ground state beyond the critical displacement field.

The energetic comparison of LPSC, SXC, and BXC states along the $U_b = 0$ line is summarized in Fig. 8. The BXC state is metastable over a broad range of E_d values, but is never the ground state. The SXC state emerges from the LPSC via a continous phase transition. As illustrated in the inset of Fig. 8 the exciton density, which is identified as the electron density transferred from the high-electric-potential bilayer to the low-electric-potential bilayer, grows continuously from zero as E_d increases beyond the value at which the LPSC becomes unstable.

We now discuss the case of larger but still moderate bilayer separation. Total energy results for $t_{\mathrm{hBN}} = 0.9$ nm, corresponding to a three-hBN-layer barrier, are illustrated in Fig. 9. (We have also performed a similar calculation for $t_{\mathrm{hBN}} = 1.8$ nm, corresponding to a six-hBN-layer barrier, which yielded results that are qualitatively similar except that phase boundaries are shifted to lower E_d.) The ground states in the small and large displacement field limits are SDW and SXC states, as in the small bilayer separation case.

For a larger value of t_{hBN}, a given displacement field yields a larger electric potential difference between the bilayers. As a result the spatially indirect band gap closes at smaller E_d values, leading to condensate formation before the isolated bilayer SDW to LPSC transition occurs. The ground state at intermediate displacement fields in this case is the 1CBXC state, in which a spatially indirect exciton condensate forms for one spin species only. We can view the effect of increasing

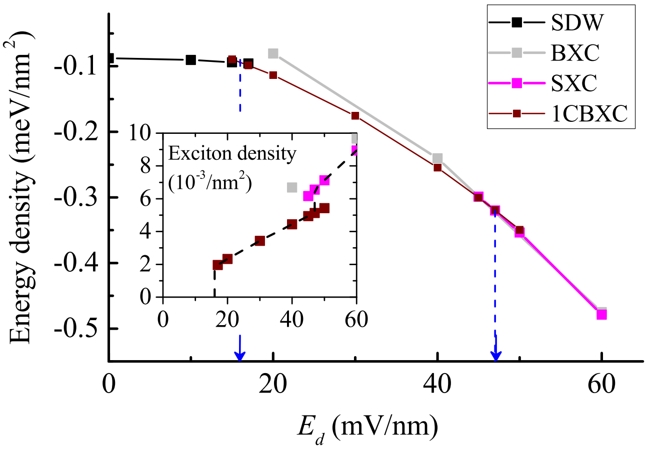

FIG. 9. Total energy vs E_d for SDW, BXC, SXC, and 1CBXC states. The inset plots the exciton densities of the SXC and BXC states. The SDW is the lowest energy state for small E_d. With increasing E_d the ground state of the system first transforms into a LPSC via a first-order phase transition and then into the SXC state via a continuous phase transition. These results were obtained for $t_{\mathrm{hBN}} = 0.9$ nm.

t_{hBN} as equivalent to an increase in U_b that is proportional to E_d, combined with a decrease in the interbilayer Coulomb interaction scale. The effective bias potential increase is $\pm eE_d\delta t_{\mathrm{hBN}}$ when the layer separation is increased by δt_{hBN}. That effective bias potential addition favors charge transfer between bilayers and the formation of exciton condensate states at smaller values of E_d. At the same time, weakening of inter-bilayer Coulomb interactions favors electron-hole pairs that form between the nearest layers in which the Coulomb interaction is maximized.

V. SPATIALLY INDIRECT EXCITON CONDENSATES IN DOUBLE BILAYER GRAPHENE: $E_d = 0$

Next we study ground state as a function of bias voltage U_b along the zero-displacement-field E_d line. U_b effectively shifts the relative energy of states in different bilayers without introducing a displacement field within the bilayers. We have compared the total energies of possible ground states with different symmetries at each U_b, as illustrated in Fig. 10. States can take advantage of U_b only by shifting charge from bilayer to bilayer. For this reason, the energies for both SDW and LPSC states are precisely constant as a function of U_b. The SDW state therefore remains the ground state until it becomes unstable when its spatially indirect exciton energy vanishes.

We define the Néel order parameter vector of a bilayer SDW state as $\vec{N} = \vec{s}_{l=1} - \vec{s}_{l=2}$, i.e., as the spin density difference between its top and bottom layers. As long as their is no single-particle tunneling between bilayers, the energy of the system is independent of the direction of either Néel vector. To simplify the following discussion we assume that the two Néel vectors are antiparallel, in the $\hat{z}$ direction in the top $n = 1$ biayer and in the $-\hat{z}$ direction in the bottom $n = 2$ bilayer. Then the $\uparrow$ valence band holes of the bilayer $n = 1$ SDW state are concentrated in layer $l = 1$ whereas the $\downarrow$ valence band holes are concentrated in layer $l = 2$. Similarly for the lower $n = 2$ bilayer the $\uparrow$ conduction band electrons are concentrated in layer $l = 3$ whereas the $\downarrow$ conduction band electrons are concentrated in layer $l = 4$. Because of the Néel order, the spatially indirect exciton energies are spin dependent, with the lowest energy excitons having the same sense of layer polarization in each bilayer.

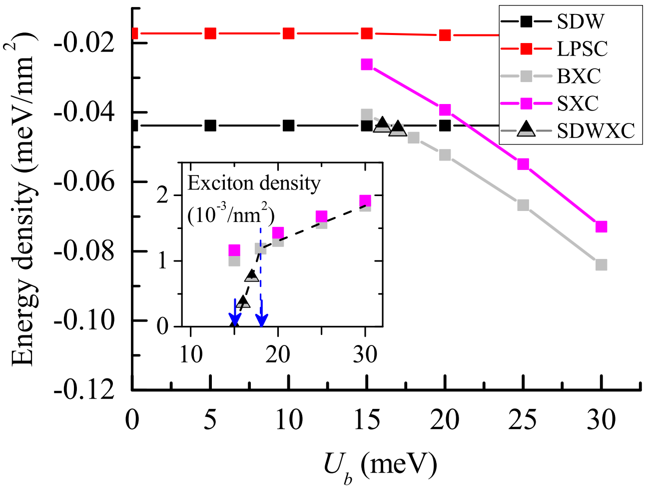

FIG. 10. Total energy vs U_b for SDW, LPSC, BXC, SXC, and SDWXC states. The inset shows exciton densities in the three states with spatially indirect condensation. The SDW is the ground state for small U_b and becomes unstable when its spatially indirect exciton energy vanishes. The exciton condensate initially breaks spin symmetry by condensing while retaining spin-density-wave order (SDWXC), but spin symmetry is restored at higher exciton density. Both SDW to SDWXC and SDWXC to BXC transitions are continuous.

The character of the SDWXC state which forms along the $E_d = 0$ line when the lowest exciton energy vanishes is illuminated by the coherence profile in Fig. 11. Because spin invariance is still broken, the coherence properties are spin dependent. For the Néel vector directions we have chosen, it follows from the discussion in the previous paragraph that the lowest energy excitons are formed between electrons whose spins are parallel in the two bilayers; $(\uparrow_e\, , \uparrow_h)$ excitons have

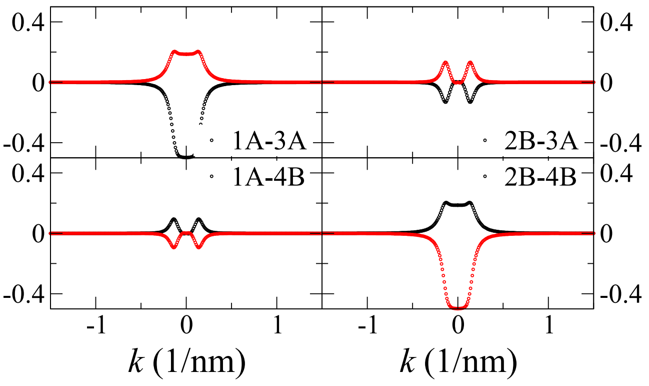

FIG. 11. Typical intersublattice coherence vs wave vector k for the SDWXC state when the Néel order parameter vectors in the two layers are along $\hat{z}$ and $-\hat{z}$ directions. The black and the red lines illustrate the coherence properties of $(\uparrow_e\, , \uparrow_h)$ and $(\downarrow_e\, , \downarrow_h)$ exciton condensates.

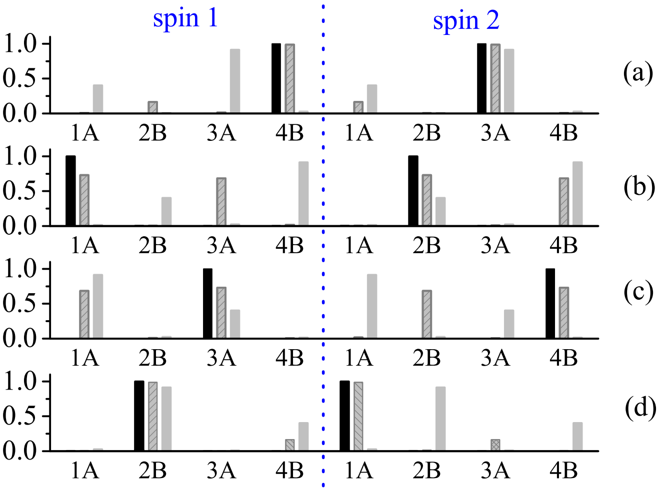

FIG. 12. Sublattice projections of SDW, SDWXC, and BXC $k = 0$ quasiparticle wave functions at $U_b = 17$ meV and $E_d = 0$ for the case in which the Néel order parameter vectors in the two layers are along $\hat{z}$ and $-\hat{z}$ directions. The top four panels are for ↑ and ↓ valence band quasiparticles, and the bottom four panels for ↑ and ↓ quasiparticles of conduction band quasiparticles. The second and third rows report projections for the bands closest to the Fermi level as in Fig. 7. The black solid, gray with slash pattern, and gray solid bars represent sublattice projections for SDW, SDWXC, and BXC states respectively.

dominant coherence between layers 1 and 3 while $(\downarrow_e , \downarrow_h)$ excitons have dominant coherence between layers 2 and 4. [Note that positive U_b favors holes in layers $l = 1{,}2$ (bilayer $n = 1$) and electrons in layers $l = 3{,}4$ (bilayer $n = 2$).] The weaker coherence between layers 2 and 4 for $(\uparrow_e , \uparrow_h)$ excitons and between layers 1 and 3 for $(\downarrow_e , \downarrow_h)$ excitons has a sign change relative to the dominant coherence because of the spin- and layer-dependent mean-field potential responsible for gaps in the SDW state has opposite sign in the two layers. This picture of the SDWXC state is reinforced in Fig. 12, where sublattice projections are compared with those of the competing BXC state that has the same value of J_X but does not break spin-rotational invariance. The phase transitions between the SDCXC state and the SDW state at small U_b, and between the SDWXC state and the BXC state at large U_b, are both continuous. The first phase transition adds spontaneous interlayer coherence to the previously established broken time-reversal symmetry, and the second phase transition drops broken time-reversal symmetry while maintaining spontaneous interlayer coherence.

Because spatially indirect excitons first condense when their total excitation energy vanishes, exciton binding energies (i.e., exciton energies relative to band gaps) can be extracted from our calculations whenever the transition to a condensed state is continuous. For example, at $E_d = 0$, the quasiparticle gap of the SDW state can be read off Fig. 3 and is ~50 meV. From Fig. 10, exciton condensation occurs at $U_b = 15$ meV. It follows that the exciton binding energy is $50 - 15 = 35$ (meV). In addition to the exciton binding energy, our calculations also provide an estimate of the exciton-exciton interaction strength at low exciton densities, which can be obtained from calculations of exciton density as a function of U_b. From the inset in Fig. 10, for example, we find that the interaction between the spatially indirect excitons of the SDW state is repulsive with strength ~17 eV nm^2.

VI. SPATIALLY INDIRECT EXCITON CONDENSATES IN DOUBLE BILAYER GRAPHENE: GENERAL CASE

In this section we briefly discuss some aspects of the phase diagram in Fig. 1 which do not emerge clearly from studies of the $U_b = 0$ and $E_d = 0$ lines. The SDW and LPSC states, which do not have spontaneous interlayer phase coherence of the XC states, are stable in the small-E_b, small-U_b corner of the phase diagram. These states are stable when the electrically controlled shift in the spatially indirect band gap is not large enough to reduce the smallest spatially indirect exciton energy to zero. There is no mechanism to allow charge transfer between bilayers in the SDW and LPSC states. XC states appear at larger U_b and E_b, because these electrical knobs both favor states that provide a mechanism for charge transfer. The broken-symmetry SDW state is favored at small E_d and the LPSC at larger E_d, as explained in Sec. III. The spatially indirect XC states appear at larger E_d and/or U_b, with large E_d favoring SXC states and large U_b favoring BXC states. The phase boundary between SXC and BXC states is first order, because the two states are distinguished by an integer-valued topological index J_X. In addition to the SDWXC intermediate state, whose stability region includes a portion of the $E_d = 0$ line, we have identified another distinct intermediate state with a stability region that does not include either the $E_d = 0$ line or the $U_b = 0$ line. For sufficiently large E_d, the transition from SDW to BXC states with increasing U_b occurs not via an intermediate SDWXC state but via a state we refer to as a 1CBXC state, in which coherence is established only for one spin component. The 1CBXC state is characterized more fully below. All phase boundaries of the 1CBXC state mark first-order phase transitions.

To shed further light on the competitions between these states we study the $E_d = 40\,\mathrm{mV/nm}$ line (line A in Fig. 1) in detail. The dependence of the ground-state energy on U_b is plotted for competing states in Fig. 13. As U_b increases the ground state evolves from a LPSU at the smallest values of U_b, to a 1CBXC mixed state at $U_b \sim 7$ meV, to a SXC state at $U_b \sim 12.5$ meV, and finally into a BXC state at $U_b \sim 14$ meV. Transitions are rarely intuitive if they occur when both E_d and U_b are finite. To compare the states before and after the transition, we define an index $S(MS1,MS2)$ which characterizes the similarity of two many-body states, $MS1$ and $MS2$. This index is computing by adding contributions from the eight $k = 0$ eigenstates ES that are closest to the Fermi surface: $S(MS1,MS2) = (1/8)\sum_{ES=1}^{8} S_{ES}$ with

$$S_{ES} = \sum_{b} \langle ES; MS1|\, b\rangle\langle b\,|ES; MS2\rangle. \qquad (7)$$

Here b is the sublattice index. S_{ES} is the inner product between $|ES; MS2\rangle$ and $MS2$ at $k = 0$. The index summarizes the information contained in the wave-function projection diagrams in a convenient way. For continuous phase transitions, $S(MS1,MS2)$ approaches one when the states are examined close to the transition. For first-order transitions, the index can differ substantially from one.

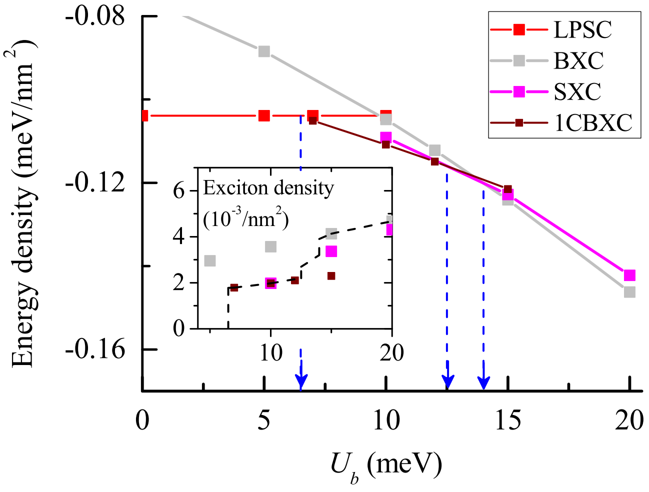

FIG. 13. Total energy vs U_b for various many body states at $E_d = 40$ mV/nm. The LPSC is lowest in energy state for small U_b. With increasing E_d the ground state of the system first turns into an intermediate 1CBXC state with broken spin symmetry and coherence, and then into a BXC state. The inset shows jumps in exciton density at the LPSC to 1CBXC transition and at the 1CBXC to BXC state transtion, demonstrating that both transitions are first order.

We now characterize the LPSC to 1CBXC transition by examining the S index and the projection diagrams of Figs. 14 and 15. These figures follow the same scheme as all previous bar diagrams; the red, brown, and gray solid bars represent the LPSC, the mixed 1CBXC state, and the BXC, respectively. These figure show first of all that one spin component of the the 1CBXC state (brown) is nonexcitonic and strongly layer polarized. At $U_b = 5$ meV the spin 1 $k = 0$ eigenstate components (Fig. 14) are identical for LPSC and the 1CBXC states. For spin 2, the highest two [Fig. 14(d)] and the lowest two [Fig. 14(a)] of the eight eigenstates are quite similar ($S_{ES} \sim 1$), whereas the two eigenstates closest to the Fermi surface [panels (b) and (c) in Fig. 14] show drastic differences ($S_{ES} \sim 0$). More specifically, we see that the 2B component of the LPSC transforms to 3A (and partly 1A) components at the transition to the 1CBXC. This difference implies charge transfer between bilayers. The small S_{ES} from these two eigenstates corresponds to an abrupt increase in exciton population at the transition, as confirmed by the inset of Fig. 13. The transition between the LPSC and the 1CBXC is first order. Increasing U_b further, we hit a second transition point. The corresponding bar diagram (Fig. 15) shows the $k = 0$ eigenstate projections for 1CBXC (brown) and BXC (gray) states. The transition from the 1CBXC state to the BXC occurs mainly on spin 1, which undergoes a transformation that is similar to that experienced by spin 2 during the LPSC to 1CBXC transition. A similar discontinuity in exciton density profile shows that hte 1CBXC to BXC transition is also a first-order phase transition. Transitions along this line have $S \sim 6/8 = 0.75$, implying that six out of eight eigenstates are very similar between before and after the transition.

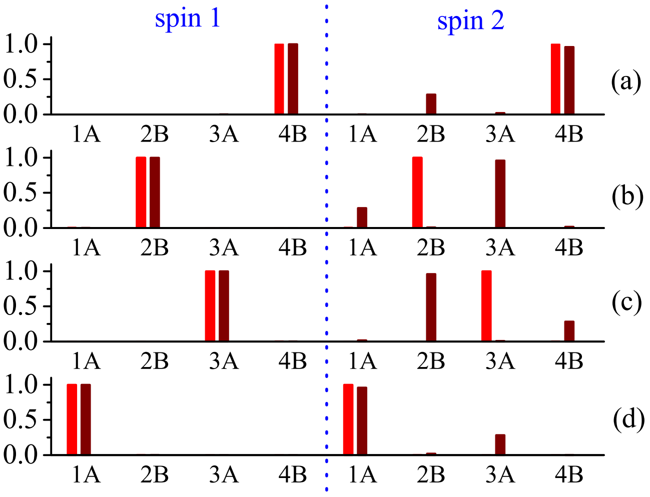

FIG. 14. Site projections of the low-energy $k = 0$ quasiparticle wave functions for $U_b = 5$ meV and $E_d = 40$ mV/nm, close to the LPSC to 1CBXC phase boundary. The red, brown, and gray solid bars represent the site quasiparticle wave-function site projections from the LPSC, 1CBXC, and BXC states respectively.

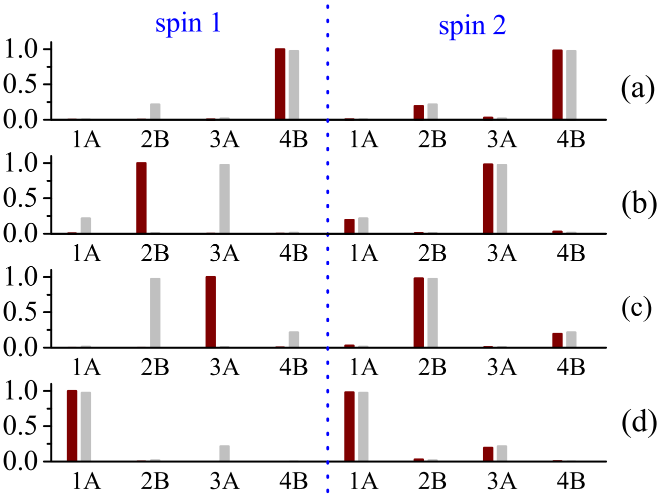

FIG. 15. Site projections of the low-energy $k = 0$ quasiparticle wave functions for $U_b = 15$ meV and $E_d = 40$ mV/nm, close to the LPSC to 1CBXC phase boundary. The brown, gray, and magenta bars represent the quasiparticle wave-function site projections from the 1CBXC, BXC, and SXC states respectively.

Next we fix the bias potential at $U_b = 10$ mV and sweep E_d (line B in Fig. 1). The energy comparison in Fig. 16 shows that at low E_d, the ground state is the SDW. Increasing E_d drives a first-order transition into the 1CBXC intermediate state at $E_d \sim 12$ mV/nm. This is followed by another transition into the SXC state at $E_d \sim 50$ eV/nm. We see from Fig. 17 that the transition from SDW to 1CBXC is first order and accompanied by a considerable charge redistribution; only the eigenstates in Figs. 17(b) and 17(d) of spin 1 and Fig. 17(d) of spin 2 have $S_{ES} \sim 1$. The charge redistribution happens both within bilayers [Figs. 17(a) and 17(c) of spin 1, Fig. 17(a) of spin 2] as well as between bilayers [Figs. 17(b) and 17(c) of spin 2], which shows that electrons move from layer 1 to 4 (holes from layers 3 to 1). The significant change results in a low S index of less than $3.5/8 = 0.4375$. A transition between 1CBXC and SXC occurs then occurs at larger E_d. By the time this

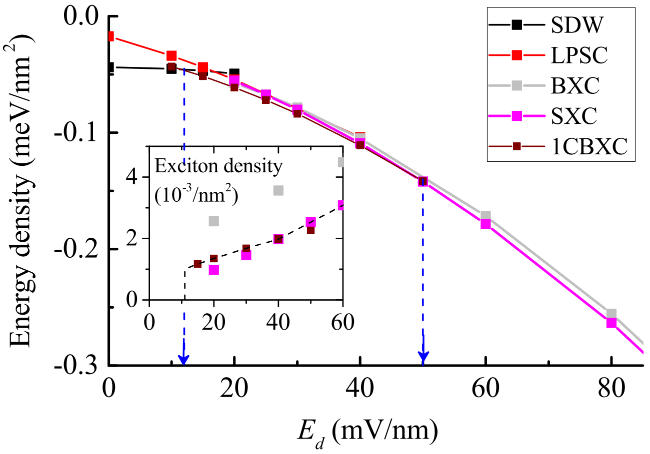

FIG. 16. Total energy vs E_d for various many-body states at $U_b =$ 10 meV; the inset shows the corresponding exciton densities. The SDW state has lowest energy for small E_d. With increasing E_d the ground-state transitions first into the mixed 1CBXC state and then into the SXC state.

phase boundary is reached the 1CBXC state has evolved into a state that is similar to the SXC state so that the transition, although first order is characterized by a value of the similarity index S that can be as large as $(4 + 4/\sqrt{2})/8 \sim 0.85$, as shown in Fig. 18. Because of the greater similarity, the transition between 1CBXC and SXC, although first order, appears to be smooth in the exciton density profile illustrated in the inset of Fig. 16.

So far we have discussed mainly results for the case of a single-layer hBN barrier which has the richest phase diagram. We now explain how the topology of the phase diagram is altered by increasing the bilayer separation. Figure 19 shows the calculated phase diagram for bilayer separation $t_{\rm hBN} = 0.9$ nm, corresponding to three-layer hBN barriers. We first note that for $E_d < 15$ mV/nm differences compared to the single-layer barrier are small. For larger E_d, the main change is that the LPSC state is absent in the three-layer barrier case. Additionally, other phases including the 1CBXC and BXC states are shifted downward toward smaller U_b compared to the single-layer phase diagram in Fig. 19. We can understand these differences by taking into consideration the two main effects of increasing layer separation. First of all, increasing $t_{\rm hBN}$ by $\delta t_{\rm hBN}$ increases the effective bias potential by $eE_d\delta t_{\rm hBN}$ because of the additional electric potential difference between bilayers at a given value of E_d. This simple shift accounts for the most of the barrier thickness dependence of the phase diagram. The small E_d SDW region of the phase diagram is therefore relatively independent of $t_{\rm hBN}$. The intermediate

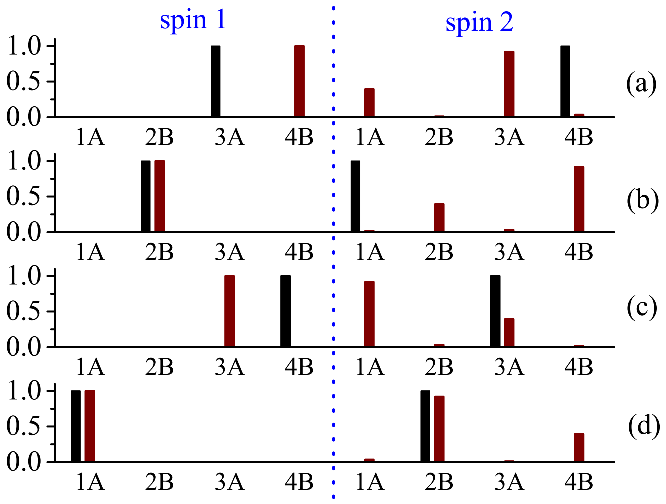

FIG. 17. Site projections of low energy $k = 0$ quasiparticle wave functions for $U_b = 10$ meV and $E_d = 15$ mV/nm. The relationship between panel position and eigenenergy order is the same as in Fig. 7. The black, brown, and magenta solid bars characterize the SDW state, the 1CBXC state, and the SXC state respectively. The Néel state order parameter vectors of the two bilayers are oppositely oriented.

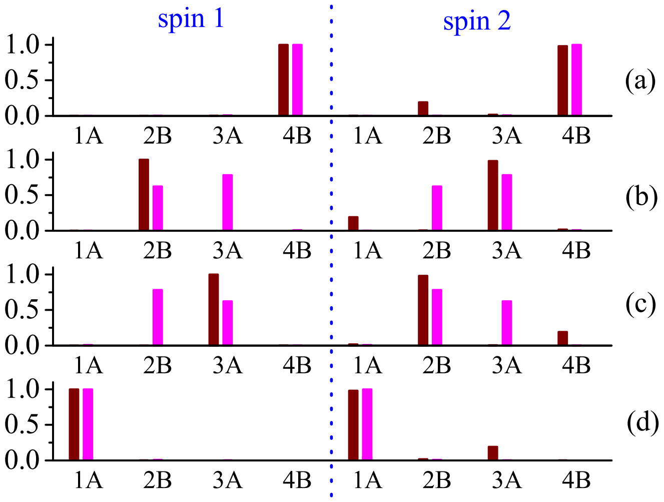

FIG. 18. Site projections of low-energy $k = 0$ eigenstates for $U_b = 10$ meV and $E_d = 50$ mV/nm, near the phase transition between 1CBXC and SXC states. The brown and magenta bars represent the 1CBXC and the SXC states, respectively.

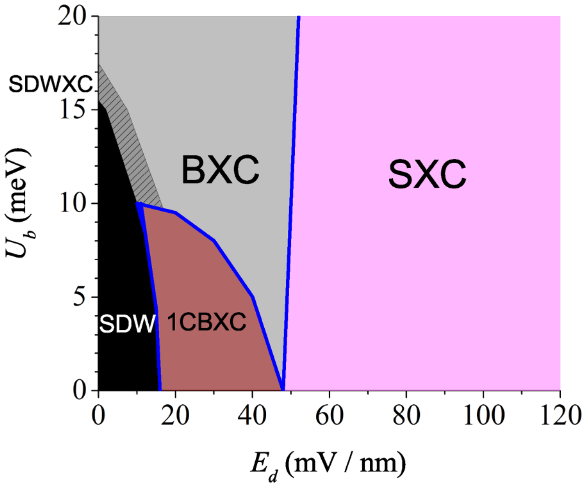

FIG. 19. Phase diagram for bilayer separation $t_{\rm hBN} = 0.9$ nm. The LPSC states do not appear because the spatially indirect exciton energy vanishes before the isolated bilayer SDW to LPSC transition occurs. The solid blue lines mark first-order phase boundaries.

state 1CBXC, on the other hand, shifts noticeably toward smaller U_b and squeezes out the LPSC. According to our calculations, the LPSC state is already entirely eliminated for the three-layer hBN barrier. In addition increasing the potential difference between bilayers, increasing t_{hBN} decreases the strength of inter-bilayer electron-electron interactions. This second effect favors SXC states over BXC states because the relative reduction in interaction strength is larger for the adjacent layers of the two-bilayer systems than for the more remote layers. The phase boundary between BXC and SXC states therefore shifts toward smaller E_d, expanding the stability range of the SCX state. We also note that at still larger t_{hBN} separations, substantial charge transfer between bilayers will occur even at small E_d, very quickly driving the double-bilayer system into a metallic Fermi liquid state.

VII. SUMMARY AND DISCUSSION

In this paper we have systematically constructed a mean-field-theory phase diagram for neutral double-bilayer graphene, demonstrating that the many-body ground state can be altered by an external displacement field E_d and an interlayer bias U_b. Mean-field theory predicts that the ground state of neutral isolated bilayers is a spin-density-wave state at $E_d = 0$ and a layer-polarized semiconductor at large E_d. These properties have already been verified experimentally. Both E_d and U_b favor charge transfer between bilayers, and this is accomplished in mean-field theory by forming excitonic condensate states that have a gap for charged excitations and spontaneous coherence between bilayers. The onset of exciton condensation occurs when the electrically tunable indirect exciton excitation energy becomes negative. The layer, sublattice, and spin degrees of freedom of graphene bilayers allow for a variety of different single-exciton states, and correspondingly for a variety of different condensate states. Distinct excitonic states can be classified by a topological quantum number J_x, related to relative angular momentum. We find that the combination of the possibility of broken time-reversal symmetry in spin-density-wave states and the possibility of condensation in different excitonic states leads to the complex phase diagram presented in Fig. 1. The phase diagram contains two types of intermediate states that combine broken spin-rotational invariance and exciton condensation in different ways.

The mean-field theory we use in this paper, which is closely related to the BCS mean-field theory of superconducting states, can capture the physics of excitons in the BEC regime and the crossover to the high exciton-density BCS regime. It does not, however, account for the metallic Fermi liquid (FL) phase generally expected [31,59] at high exciton densities. The FL phase, like the exciton condensate, has charge transfer between bilayers, but does not support broken symmetries of charge-excitation gaps. Because these simple Fermi liquid states are not predicted by mean-field theory, in which condensation always occurs when excitons are present, we have chosen not to represent them explicitly in Fig. 1. Metallic Fermi liquid double bilayer excitonic states are expected when the density of excitons times the area occupied by a spatially indirect exciton bound state is large, in other words when excitons overlap strongly, and therefore should appear along the upper right of the phase diagram in Fig. 1 as indicated schematically in Fig. 20. Another possible phase that is not described by the mean-field theory is the biexciton phase [59], in which excitons pair to form bound biexcitons, which are analogs of hydrogen molecules. In mean-field theory, the interactions between excitons is always repulsive. The attractive interaction that can result from fluctuating dipoles can in principle produce attraction. This effect is unlikely to be important at finite E_d, however, because the dipole orientations are fixed by displacement fields.

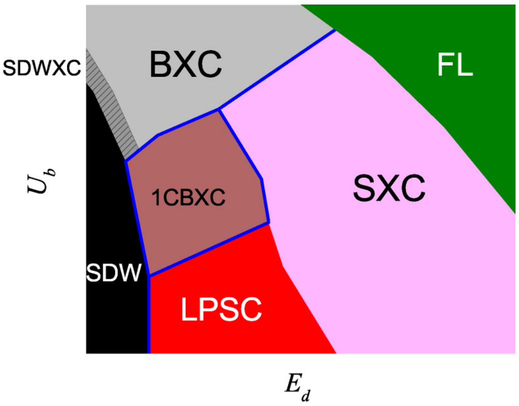

FIG. 20. Schematic phase diagram including Fermi liquid (FL) states. The mean-field theory instability of Fermi liquid states toward states with spontaneous coherence between bilayers is expected to be suppressed by correlations at high exciton densities.

The excitonic condensates proposed in this paper are normally most conveniently identified in experiment by performing drag measurements, since spontaneous coherence in an exciton state shorts electrical isolation and eliminates layer dependence of measured voltages, even when separate contacting is well established experimentally. In a double bilayer drag experiment current flows through one bilayer and voltage drops are measured both in the bilayer carrying the transport current (the drive layer) and in the adjacent electrically isolated bilayer (the drag layer). Consider, for example, the $E_d = 0$ case. At $U_b = 0$ both drag and drive layers are expected to be in SDW states if disorder is sufficiently weak. The resistance measured in an isolated neutral bilayer in an SDW state should therefore be large and increase indefinitely as temperature is lowered. (Importantly, this property contrasts with the extensively studied spatially-indirect-condensate case of semiconductor double quantum well systems in a magnetic field, where coherence is established between layers in $\nu = 1/2$ quantum Hall states. Although the quantum Hall spatially indirect condensate state has a bulk gap, it also has topologically protected edge states and therefore has a finite longitudinal resistance as temperature goes to zero.) By increasing U_b the spatially indirect exciton energies can be tuned to zero, allowing excitons to be present in the system in equilibrium. We predict that when the exciton density is low, spontaneous interlayer coherence will be established between the bilayers and the resistive voltage drop measured in the direction of current flow will be detected by voltage probes connected to either bilayer.

We emphasize that there is a qualitative difference between double bilayer graphene and double monolayer graphene [60–67] that is relevant to their ability to host robust spatially indirect exciton condensates. Because the bilayer is a semiconductor, it has a band of elementary neutral excitations, the exciton states, that lie below the particle-hole excitation spectrum continuum. As long as the density of excitons is low, the argument that they can be considered to be weakly interacting bosons is straightforward and reliable. The weakly interacting low-exciton-density limit is accurately captured by the mean-field approximation that we employ, whereas quantum fluctuations become more important at higher exciton densities. It is generally expected that the true ground state at high exciton densities is a Fermi liquid, as discussed in the previous paragraph, although quantitative calculations remain a challenge. At a minimum the critical temperature in this limit is expected to be reduced because electron-hole interactions are screened [63,64,67,68], Because monolayer graphene is a gapless semiconductor, its particle-hole excitation continuum does not have a lower bound and there are therefore no isolated bosonic excitations. Similarly, in double monolayer graphene there are no isolated spatially indirect exciton excited states [66]. The low-density regime in which more quantitative theoretical predictions are possible is absent in the double monolayer case. Because of its electrically tunable gaps, the double bilayer provides an interesting opportunity to explore the crossover between the rather simple case of spatially indirect condensates formed between two-dimensional semiconductors and the more complex case of spatially indirect exciton condensates in gapless systems, which is approached for small displacement fields.

Although this work has restricted its attention to the physics of neutral double bilayers, it seems clear that interbilayer electron-electron interactions can also have a strong influence on double-bilayer properties away from charge neutrality, particularly when the carrier density in one bilayer or the other is low and the Fermi level lies close to the Mexican hat features in the quasiparticle dispersion that are evident in the quasiparticle band dispersions plotted in this article. A number of recent experimental papers [29–33] with intriguing findings demonstrate the potential for interesting many-electron physics in the double bilayer system, a part of which is addressed here, leaving many avenues for future theoretical and experimental work.

ACKNOWLEDGMENTS

We thank M. Allen, C. Dean, P. Kim, C. N. Lau, J. Li, X. Liu, F. Wang, A. Yacoby, and A. Young for valuable interactions. J.-J.S. acknowledges the supports by Ministry of Science and Technology (MOST 102-2112-M-009-018-MY3) and by National Center for Theoretical Sciences of Taiwan. Work at Austin was supported by the Department of Energy, Office of Basic Energy Sciences under Contract No. DE-FG02-ER45118 and by the Welch foundation under Grant No. TBF1473.

---

[1] E. McCann and V. I. Falko, Phys. Rev. Lett. **96**, 086805 (2006).

[2] T. Ohta, A. Bostwick, T. Seyller, K. Horn, and E. Rotenberg, Science **313**, 951 (2006).

[3] E. McCann, Phys. Rev. B **74**, 161403 (2006).

[4] J. B. Oostinga, H. B. Heersche, X. L. Liu, A. F. Morpurgo, and L. M. K. Vandersypen, Nat. Mater. **7**, 151 (2007).

[5] E. V. Castro, K. S. Novoselov, S. V. Morozov, N. M. R. Peres, J. M. B. Lopes dos Santos, J. Nilsson, F. Guinea, A. K. Geim, and A. H. Castro Neto, Phys. Rev. Lett. **99**, 216802 (2007).

[6] H. Min, B. Sahu, S. K. Banerjee, and A. H. MacDonald, Phys. Rev. B **75**, 155115 (2007).

[7] J. Nilsson and A. H. Castro Neto, Phys. Rev. Lett. **98**, 126801 (2007).

[8] Y. Zhang *et al.*, Nature (London) **459**, 820 (2009).

[9] R. Dillenschneider and J. H. Han, Phys. Rev. B **78**, 045401 (2008).

[10] K. F. Mak, C. H. Lui, J. Shan, and T. F. Heinz, Phys. Rev. Lett. **102**, 256405 (2009).

[11] C.-H. Park and S. G. Louie, Nano Lett. **10**, 426 (2010).

[12] J. P. Eisenstein and A. H. MacDonald, Nature (London) **432**, 691 (2004).

[13] J. P. Eisenstein, Annu. Rev. Condens. Matter Phys. **5**, 159 (2014).

[14] J.-J. Su and A. H. MacDonald, Nat. Phys. **4**, 799 (2008).

[15] J.-J. Su and A. H. MacDonald, Phys. Rev. B **81**, 184523 (2010).

[16] D. A. Pesin and A. H. MacDonald, Phys. Rev. B **84**, 075308 (2011).

[17] Y.-F. Hsu and J.-J. Su, Sci. Rep. **5**, 15796 (2015).

[18] X. Huang, W. Dietsche, M. Hauser, and K. von Klitzing, Phys. Rev. Lett. **109**, 156802 (2012), and work cited therein.

[19] D. Nandi, T. Khaire, A. D. K. Finck, J. P. Eisenstein, L. N. Pfeiffer, and K. W. West, Phys. Rev. B **88**, 165308 (2013); D. Nandi, A. D. K. Finck, J. P. Eisenstein, L. N. Pfeiffer, and K. W. West, Nature (London) **488**, 481 (2012).

[20] I. Sodemann, H. Chen, and A. H. MacDonald, arXiv:1411.0008 (unpublished).

[21] P. Maher, Nat. Phys. **9**, 154 (2013).

[22] C. N. Lau, Nat. Phys. **9**, 135 (2013), and work cited therein.

[23] We neglect the possibility of broken valley symmetries. When this type of broken symmetry is allowed, it is possible that intermediate anomalous quantum Hall states occurs over a range of displacement fields.

[24] L. Yang, J. Deslippe, C.-H. Park *et al.*, Phys. Rev. Lett. **103**, 186802 (2009); L. Yang, Phys. Rev. B **81**, 155445 (2010); **83**, 085405 (2011); Y. Liang and L. Yang, *ibid.* **86**, 205423 (2012).

[25] O. Berman, R. Y. Kerzashvili, and K. Ziegler, Phys. Rev. B **85**, 035418 (2012).

[26] B. Seradjeh, H. Weber, and M. Franz, Phys. Rev. Lett. **101**, 246404 (2008).

[27] D. I. Pikulin, P. G. Silvestrov, and T. Hyart, Nat. Commun. **7**, 10462 (2016).

[28] B. Seradjeh, J. E. Moore, and M. Franz, Phys. Rev. Lett. **103**, 066402 (2009).

[29] J. I. A. Li, T. Taniguchi, K. Watanabe, J. Hone, A. Levchenko, and C. R. Dean, Phys. Rev. Lett. **117**, 046802 (2016).

[30] X. Liu, T. Taniguchi, K. Watanabe, and P. Kim (unpublished).

[31] A. Perali, D. Neilson, and A. R. Hamilton, Phys. Rev. Lett. **110**, 146803 (2013).

[32] M. Zarenia, A. Perali, D. Neilson, and F. M. Peeters, Sci. Rep. **4**, 7319 (2014).
[33] K. Lee, J. Xue, D. C. Dillen, K. Watanabe, T. Taniguchi, and E. Tutuc, Phys. Rev. Lett. **117**, 046803 (2016).
[34] R. Bistritzer and A. H. MacDonald, Phys. Rev. B **81**, 245412 (2010).
[35] J. Velasco *et al.*, Nat. Nano. **7**, 156 (2012).
[36] G.-H. Lee, Y.-J. Yu, C. Lee, C. Dean, K. L. Shepard, P. Kim, and J. Hone, Appl. Phys. Lett. **99**, 243114 (2011).
[37] L. Britnell *et al.*, Nano Lett. **12**, 1707 (2012).
[38] K. Kim *et al.*, Nano Lett. **16**, 1989 (2016).
[39] M. T. Mihnev *et al.*, Nat. Commun. **6**, 8105 (2015).
[40] J. C. W. Song and L. S. Levitov, J. Phys.: Condens. Matter **27**, 164201 (2015).
[41] R. Bistritzer and A. H. MacDonald, Phys. Rev. Lett. **102**, 206410 (2009).
[42] A. Imamoglu, R. J. Ram, S. Pau, and Y. Yamamoto, Phys. Rev. A **53**, 4250 (1996); J. Kasprzak *et al.*, Nature (London) **443**, 409 (2006); S. Christopoulos, G. Baldassarri Höger von Högersthal, A. J. D. Grundy, P. G. Lagoudakis, A. V. Kavokin, J. J. Baumberg, G. Christmann, R. Butté, E. Feltin, J.-F. Carlin, and N. Grandjean, Phys. Rev. Lett. **98**, 126405 (2007); R. Balili, V. Hartwell, D. Snoke, L. Pfeiffer, and K. West, Science **316**, 1007 (2007); A. Amo *et al.*, Nature (London) **457**, 291 (2009); For review, see, for example, Deng, H. Haug, and Y. Yamamoto, Rev. Mod. Phys. **82**, 1489 (2010); T. Byrnes, N. Y. Kim, and Y. Yamamoto, Nat. Phys. **10**, 803 (2014), and work cited therein.
[43] Y. Jang, E. H. Hwang, A. H. MacDonald, and H. Min, Phys. Rev. B **92**, 041411(R) (2015); J. Zhang and E. Rossi, Phys. Rev. Lett. **111**, 086804 (2013).
[44] H. Min and A. H. MacDonald, Phys. Rev. B **77**, 155416 (2008).
[45] J. Jung and A. H. MacDonald, Phys. Rev. B **89**, 035405 (2014), and work cited therein.
[46] R. T. Weitz, M. T. Allen, B. E. Feldman, J. Martin, and A. Yacoby, Science **330**, 812 (2010).
[47] A. S. Mayorov *et al.*, Science **333**, 860 (2011).
[48] F. Freitag, J. Trbovic, M. Weiss, and C. Schoenenberger, Phys. Rev. Lett. **108**, 076602 (2012).
[49] A. Veligura, H. J. van Elferen, N. Tombros, J. C. Maan, U. Zeitler, and B. J. van Wees, Phys. Rev. B **85**, 155412 (2012).
[50] W. Bao *et al.*, Proc. Natl. Acad. Sci. U.S.A. **109**, 10802 (2012).
[51] E. V. Castro, N. M. R. Peres, T. Stauber, and N. A. P. Silva, Phys. Rev. Lett. **100**, 186803 (2008).
[52] Y. Lemonik, I. L. Aleiner, C. Toke, and V. I. Falko, Phys. Rev. B **82**, 201408(R) (2010).
[53] E. V. Gorbar, V. P. Gusynin, and V. A. Miransky, Phys. Rev. B **81**, 155451 (2010).
[54] F. Zhang, J. Jung, G. A. Fiete, Q. Niu, and A. H. MacDonald, Phys. Rev. Lett. **106**, 156801 (2011).
[55] F. Zhang and A. H. MacDonald, Phys. Rev. Lett. **108**, 186804 (2012).
[56] A. H. MacDonald, J. Jung, and F. Zhang, Phys. Scr. **T146**, 014012 (2012).
[57] To consider the interbilayer screening process to the random phase approximation (RPA) level, for example, we will have to include also a set of bubble diagrams in which the electron and hole are from different bilayers. However, since the density distribution in each layer varies greatly in different regions in the phase diagram, that will require a self-consistent treatment for screening, e.g., the one in Stroucken *et al.*, Phys. Rev. B **87**, 245428 (2013).
[58] M. Combescot, R. Combescot, M. Alloing, and F. Dubin, Phys. Rev. Lett. **114**, 090401 (2015); F.-C. Wu, F. Xue, and A. H. MacDonald, Phys. Rev. B **92**, 165121 (2015), and work cited therein.
[59] R. Maezono, P. López Ríos, T. Ogawa, and R. J. Needs, Phys. Rev. Lett. **110**, 216407 (2013).
[60] H. Min, R. Bistritzer, J.-J. Su, and A. H. MacDonald, Phys. Rev. B **78**, 121401(R) (2008).
[61] Yu. E. Lozovik and A. A. Sokolik, JETP Lett. **87**, 55 (2008).
[62] R. Bistritzer and A. H. MacDonald, Phys. Rev. Lett. **101**, 256406 (2008).
[63] M. Yu. Kharitonov and K. B. Efetov, Phys. Rev. B **78**, 241401(R) (2008).
[64] R. Bistritzer, H. Min, J.-J. Su, and A. H. MacDonald, arXiv:0810.0331 (unpublished).
[65] M. P. Mink, H. T. C. Stoof, R. A. Duine, and A. H. MacDonald, Phys. Rev. B **84**, 155409 (2011).
[66] Yu. E. Lozovik, S. L. Ogarkov, and A. A. Sokolik, Phys. Rev. B **86**, 045429 (2012).
[67] M. V. Fischetti, J. Appl. Phys. **115**, 163711 (2014).
[68] D. Neilson, A. Perali, and A. R. Hamilton, Phys. Rev. B **89**, 060502(R) (2014).